Reconstructing Tissue Properties from Medical Images with Application in Cancer Screening

Shan Yang, Junbang Liang, Vladimir Jojic, Jun Lian, Ronald C. Chen, and Ming C. Lin, *Fellow, IEEE*

***Abstract*— Purpose: In this paper, we describe a method for recovering the tissue properties directly from medical images and study the correlation of tissue (i.e. prostate) elasticity with the aggressiveness of prostate cancer using medical image analysis.**
Methods: We present a novel method that uses geometric and physical constraints to deduce the relative tissue elasticity parameters. Although elasticity reconstruction, or elastograph, can be used to estimate tissue elasticity, it is less suited for in-vivo measurements or deeply seated organs like prostate. We develop a method to estimate tissue elasticity values based on pairs of images, using a finite-element based biomechanical model derived from an initial set of images, local displacements and an optimization-based framework.
Results: We demonstrate the feasibility of a statistically based classifier that automatically provides a clinical T-stage and Gleason score based on the elasticity values reconstructed from computed tomography (CT) images.
Conclusions: We study the relative elasticity parameters by performing cancer Grading/Staging prediction and achieve up to 85% accuracy for cancer Staging prediction and up to 77% accuracy for cancer Grading prediction using feature set which includes recovered relative elasticity parameters and patient age information.

***Index Terms*— Physically-based Simulation, Elasticity Recovery**

I. Introduction

Medical robots have the potential to perform surgical procedures beyond current clinical capabilities. To enable medical robots to safely operate within highly unstructured, deformable human bodies and to compute desired and accurate force feedback for haptic display requires knowledge about the deformation of soft tissues and organs, which are characterized by patient-specific elastic parameters. In addition to medical robots, surgical simulation are also increasingly used for rapid prototyping of clinical devices, pre-operation planning of medical procedures, virtual training exercises for surgeons and supporting personnel, etc.

Tissue elasticity properties are important parameters for developing realistic and predictive surgical simulation and for designing responsive and dexterous surgical manipulators. Furthermore, studies have shown that the tissue stiffness described by the tissue properties may indicate abnormal pathological process. Ex-vivo, measurement-based methods, such as [1], [2] using magnetic resonance imaging (MRI) and/or ultrasound, were proposed for study of prostate cancer tissue. However, previous works in material property reconstruction often have limitations with respect to their genericity, applicability, efficiency, accuracy, and costs [3]. More recent techniques, such as inverse finite-element methods [3]–[7], stochastic finite-element methods [8], and image-based ultrasound [9] have been developed for in-vivo soft tissue analysis, when cost consideration is involved (e.g. using CT instead of MRI).

In this paper, we present an improved method that uses geometric and physical constraints to deduce the relative tissue elasticity parameters. Although elasticity reconstruction, or elastography, can be used to estimate tissue elasticity, it is less suited for in-vivo measurements or deeply seated organs like prostate. We describe a non-invasive method to estimate tissue elasticity values based on pairs of CT images, using a finite-element based biomechanical model derived from an initial set of images, local displacements, and an optimization-based framework. To demonstrate its potential use, we further study the possible use of tissue (i.e. prostate) elasticity to evaluate the prognosis of prostate cancer patients, given at least two set of CT images. The clinical T-stage of a prostate cancer is a measure of how much the tumor has grown and spread; while a Gleason score based on the biopsy of cancer cells indicates aggressiveness of the cancer. They are commonly used for cancer staging and grading.

Given the recovered tissue properties reconstructed from analysis of medical images and patient's ages, we develop a multiclass classification system for predicting clinical T-stage and Gleason scores for prostate cancer patients. We demonstrate the feasibility of a statistically-based multiclass classifier that predicts a supplementary assessment on cancer T-stages and cancer grades using the computed elasticity values from medical images, as an additional clinical aids for the physicians and patients to make more informed decision (e.g. more strategic biopsy locations, less/more aggressive treatment, etc). Concurrently, extracted image features [10]–[12] using dynamic contrast enhanced (DCE) MRI have also been suggested for prostate cancer detection. These methods are complementary to ours and can be used in conjunction with ours as a multimodal classification method to further improve the overall prediction accuracy.

II. Related Work

Image-based Deformable-body Material Properties Reconstruction Researchers have proposed different methods for reconstructing material parameters from images and videos, from model-based optimization [13] to data-driven machine

learning methods [14]. We use a simulation-optimization framework, optimizing the physical properties of the deformable body in order to match the target shape as closely as possible. We extend the work from [15] by nearly tripling the training data, and by more in-depth comparison to demonstrate the effectiveness of the approach.

Bio-Tissue Modeling Bio-tissue modeling has been extensively studied by many researchers. We refer readers to this nice survey on bio-tissue modeling in medical simulations [16]. The survey summed up the three generations so far for the research in the bio-tissue modeling in medical simulation. The first generation simulators only consider the geometrical nature of human tissue. The second one focuses on the physical interaction of the bio-tissue, after which the last generation can already include the functional of the human organs. Commonly used bio-tissue modeling methods include mass-spring model and finite element methods. Mass-spring model is known to be fast but low in accuracy. Finite element method becomes more and more commonly used because of the better precision and the increase in the computation resources.

Hyperelastic Material Model Material model plays a vital role in bio-tissue simulation. Material model can be roughly divided in to two classes, linear and nonlinear material models, differing on the relationship between the stress and the strain [17]. For many materials, linear elastic models cannot accurately capture the observed material behavior; hyperelastic material models that can capture the nonlinear material behavior are widely used when the object is subjected to large strain. For example, animal tissue and some common organic materials are often simulated using hyperelastic material. In this project we choose to use hyperelastic material model.

III. Method

Given two sets of multi-view images of a deformable object, our framework can automatically estimate relative elasticity properties of it. We assume that (at least) two sets of multiple-view images are given, along with some initial guess at the elasticity parameters. We first reconstruct the 3D geometry from the images, and in the meanwhile generate the subregions of the object for computing the subjected traction force. Based on the traction force, we apply a simulation-optimization framework, consisting of the **forward simulation** and the **inverse optimization**, to compute the best set of elasticity parameters that yields the deformed shape with the minimal difference compared to the target object. Finally using the estimated relative elasticity parameter we train a classifier to the desired cancer prognostic scores.

A. Geometry Reconstruction and Mesh Generation

There are many approaches to reconstructing 3D geometry from multiple images; the method chosen depends upon the image sources. We briefly summarize below how the 3D geometry of input objects can be constructed using various image sources.

Medical Images are usually taken when the organs are in a static or quasi-static state. There are several widely-used imaging technologies, such as X-ray radiography, magnetic resonance imaging (MRI), medical ultrasonography or ultrasound, elastography, tactile imaging, thermography, nuclear medicine functional imaging, computed tomography (CT) scanning or computerized axial tomography (CAT), etc. Each set of CT or CAT scans provides image "slices", or the cross-sectional images of anatomy. Variants of MRI and ultrasound images can be used to reconstruct anatomical 3D geometry using public-domain libraries such as ITK-SNAP [18] or commercial systems such as AVS, 3D-Doctor, MxAnatomy, etc.

2D Drawings and Sketches can be converted to 3D models using widely available commercial CAD and 3D modeling systems, such as Rhino, Autodesk LABS, Dassault Systems SolidWorks, etc.

Multi-view Images from Cameras/Camcorder and other imaging technologies have been used for 3D geometry reconstruction. Excellent surveys of methods of extracting 3D models from images can be found in [18]–[21]. These methods include algorithms using images for which camera parameters are unknown, uncalibrated structure-from-motion methods, metric reconstruction from images with additional knowledge about images, etc.

FEM Mesh Generation is accomplished by first building the input surface meshes as described above. If medical images (e.g. CT, MRI, etc.) are used as input they require an additional step before mesh generation: segmenting using ITK-SNAP [18] into multiple regions. After mesh simplification and smoothing, the entire region of interest can be tetrahedralized using TetGen [22].

B. Forward Simulation: Bio-Tissue Modeling

This step uses the elasticity parameters generated from the inverse optimization process to compute the amount of deformation that the body would undergo. We use the FEM to solve the following governing equation of the deformable body.

$$\begin{aligned}&\int_\Omega \delta\mathbf{u}^T\rho\ddot{\mathbf{u}}\,\mathrm{d}\Omega+\int_\Omega \delta(\boldsymbol{\varepsilon})^T\boldsymbol{\sigma}\,\mathrm{d}\Omega\\&-\int_\Omega \delta\mathbf{u}^T\mathbf{b}\,\mathrm{d}\Omega-\int_\Gamma \delta\mathbf{u}^T\mathbf{t}\,\mathrm{d}\Gamma=0,\end{aligned}\tag{1}$$

with $\mathbf{u}$ as the displacement field, $\boldsymbol{\varepsilon}$ as the strain tensor, $\boldsymbol{\sigma}$ as the stress tensor, $\mathbf{b}$ as the body force and $\mathbf{t}$ as the tractions on the boundary Γ of the deformable body Ω. For the quasi-static deformation process the $\ddot{\mathbf{u}}=\mathbf{0}$. We can rewrite Eqn. 1 as

$$\left[\int_\Omega \delta(\boldsymbol{\varepsilon})^T\boldsymbol{\sigma}\,\mathrm{d}\Omega-\int_\Omega \delta\mathbf{u}^T\mathbf{b}\,\mathrm{d}\Omega\right]-\left[\int_\Gamma \delta\mathbf{u}^T\mathbf{t}\,\mathrm{d}\Gamma\right]=0,\tag{2}$$

with the first part of the equation as the internal body force and the second part as the external force. The computation of the stress force is determined by the material properties. Researchers have proposed many models for simulating different kinds of materials. These material models define the relation between the stress and the strain. To simulate the human organs in the abdomen and the soft tissue surrounding those organs, we use the isotropic hyperelastic material model,

which is used commonly to approximate the deformation behavior of human tissue [23]. The stress-strain relation for the hyperelastic material model is defined through the strain energy density function $\mathbf{\Psi}$ (energy per unit undeformed volume). We will be using the Green-Lagrange strain tensor $\mathbf{E}$ with the second Piola-Kirchhoff stress tensor $\boldsymbol{\sigma}^{\text{PK2}}$ [24]. The boundary conditions we apply are the tractions $\mathbf{t}$ applied on the boundary Γ. Our forward simulation framework uses an invertible FEM [25] to ensure that the deformed elements have positive volumes in the coupled simulation-optimization process.

1) Material Model: The elastic behavior of deformable bodies varies for different materials. For small deformations, most elastic materials (e.g. springs) exhibit linear elasticity, which can be described as a linear function between stress and strain.

Linear Elasticity Material Model: The linearly elastic model assumes a constant variation of stress and strain according to Hooke's law, with no permanent deformations after the applied stresses are removed. This holds true until the yield point, which is followed by an unrestricted plastic strain after yield. Assuming isotropic linear elasticity, we can write

$$\boldsymbol{\sigma} = \mathbf{D}\boldsymbol{\varepsilon}, \tag{3}$$

where $\boldsymbol{\sigma}$ is the stress tensor induced by the *surface forces*, $\boldsymbol{\varepsilon}$ is the strain tensor defined by the deformation gradient, and $\mathbf{D}$ is a matrix defined by the material property parameters $\boldsymbol{\mu}$ ($\mathbf{D} = \mathbf{D}(\boldsymbol{\mu})$). Assuming an isotropic material, the commonly used material property parameters are Young's modulus E and Poisson's ratio ν.

Isotropic Nonlinear Hyperelastic Material Model: For many materials, linear elastic models cannot accurately capture the observed material behavior. Hyperelastic material models better describe the nonlinear material behavior exhibited when deformable bodies are subjected to large strains. For example, animal tissue and some common organic materials are known to be hyperelastic [23]. The nonlinearity is captured through the energy density function $\mathbf{\Psi}$ for hyperelastic material models. The energy function is a function of the strain tensor $\boldsymbol{\varepsilon}$ and the material property parameters $\boldsymbol{\mu}$, where $\mathbf{\Psi} = \mathbf{\Psi}(\boldsymbol{\varepsilon}, \boldsymbol{\mu})$. With the energy function, the stress tensor is computed by taking the derivative of the energy function over the strain tensor.

$$\boldsymbol{\sigma} = \frac{\partial \mathbf{\Psi}(\boldsymbol{\varepsilon}, \boldsymbol{\mu})}{\partial \boldsymbol{\varepsilon}} \tag{4}$$

The energy function takes different forms for different models of hyperelastic materials.

Energy Function: The energy density function determines the nonlinear behavior of the deformable object. Human organs are hyperelastic and nearly isotropic. Generally speaking, for an isotropic material model, the energy function is expressed as a function of the invariants $\mathbf{I}_1$, $\mathbf{I}_2$ and $\mathbf{I}_3$ of the deformation gradient $\mathbf{F}$,

$$\begin{aligned} \mathbf{I}_1 &= \lambda_1^2 + \lambda_2^2 + \lambda_3^2 \\ \mathbf{I}_2 &= \lambda_1^2\lambda_2^2 + \lambda_2^2\lambda_3^2 + \lambda_1^2\lambda_3^2 \\ \mathbf{I}_3 &= \lambda_1^2\lambda_2^2\lambda_3^2 \end{aligned} \tag{5}$$

and the deformation gradient $\mathbf{F}$ is a function of the strain $\mathbf{F} = \mathbf{F}(\boldsymbol{\varepsilon})$. One general energy function for this class of incompressible materials, proposed by Rivlin [26], is

$$\mathbf{\Psi_R} = \sum_{i,j=0}^{\infty} \mathbf{C}_{ij}(\mathbf{I}_1 - 3)^i(\mathbf{I}_2 - 3)^j, \tag{6}$$

where $\mathbf{C}_{ij}$ are the material parameters. To account for volume changes, compressible forms of this class of material are proposed by adding the third invariant to the above Rivlin expression.

$$\mathbf{\Psi} = \mathbf{\Psi_R} + \mathbf{\Psi}(\mathbf{J}), \tag{7}$$

where $\mathbf{J}$ is the volume ratio $\mathbf{J} = \sqrt{\mathbf{I}_3}$.

Mooney-Rivlin material model is widely known for its accuracy in modeling this property; we use this model in our implementation because of its popularity and wide adoption in both medical and engineering applications. In this paper, we use this form of the energy function of Mooney-Rivlin material model [27], [28]:

$$\mathbf{\Psi} = \frac{1}{2}\mu_1((\mathbf{I}_1^2 - \mathbf{I}_2)/\mathbf{I}_3^{\frac{2}{3}} - 6) + \mu_2(\mathbf{I}_1/\mathbf{I}_3^{\frac{1}{3}} - 3) + v_1(\mathbf{I}_3^{\frac{1}{2}} - 1)^2, \tag{8}$$

where μ_1, μ_2 and v_1 are the material parameters. The first two elasticity parameters, μ_1 and μ_2, are related to the distortional response (i.e., together they describe the response of the material when subject to shear stress, uniaxial stress, and equibiaxial stress), while the last parameter, v_1, is related to volumetric response (i.e., it describes the material response to bulk stress).

Incompressibility: In our simulation, we model abdominal organs as incompressible material [29]. There are several options for achieving incompressibility: One can add constraints to the governing equation to ensure that the determinant of the jacobian $\mathbf{J}$ of the deformation gradient $\mathbf{F}$ is equal to one. Alternatively, one can use the third material parameter (v_1 in Eqn. 8) to approximate incompressibility. To achieve incompressibility, we choose a fairly large v_1; this means v_1 will not be optimized. In order to accurately describe the material, we reconstruct both μ_1 and μ_2.

2) The Boundary Condition : The boundary condition is critical in solving Eqn. 2. The boundary condition can be either the displacement field or the tractions on the boundary. Our target applications for this work include both medical applications and sketch-driven animation; for medical applications, we use the contact force between the organ and the surrounding tissue as the boundary condition. To compute the contact force we make two assumptions:

1) We simulate the surrounding tissue using a linear material model.
2) We know the (default) elasticity parameters for the surrounding tissue.

During the model reconstruction step, we include the surrounding soft tissue of the prostate, as well as the bones of the male pelvis area (as shown in Fig. 2). We simulate the surrounding tissue using a linear material model. This assumption is valid because the volume of the surrounding tissue is far larger than that of the target organ, so the amount of strain $\frac{\partial \mathbf{u}_s}{\partial \mathbf{X}_s}$ can be considered a small strain. The displacement of the surface of the surrounding tissue will populate the displacement field $\mathbf{u}_s$. For the second assumption, we set the elasticity parameters of

the surrounding tissue to a default value. Then the elasticity parameters of the target organ become *relative* values with respect to the surrounding tissue. The second assumption is necessary for several reasons:

1) It is almost impossible to assess the elasticity properties of the tissue surrounding the target organ *in vivo*;
2) without the boundary condition we cannot accurately solve the governing equation, Eqn. 2; and
3) the relative material properties of the target organ, being able to normalize the per-patient fluctuation in absolute elasticity values due to varying degrees of hydration and other temporary factors, have already proven to be useful for cancer detection [30].

Given the displacement field $\mathbf{u}_s$ of the surrounding tissue, we compute the contact force using the following equation:

$$\mathbf{K}\mathbf{u}_s = \mathbf{f}, \tag{9}$$

where $\mathbf{K}$ is the stiffness matrix of the surrounding tissue (whose elasticity parameters are known), and $\mathbf{f}$ is the resulting contact force. Friction does not have a notable impact on our experimental results and also has little impact in practice between organs, so we did not model friction in the simulation. The FEM domain for the computation consists of elements belonging only to the surrounding tissue. An example of the reconstructed contact force is shown in Fig. 2a.

3) Generalized Minimal Residual Solver: Classical iterative solvers such as the stationary iterative method Jacobi are suitable for well-conditioned linear system, such as the generalized conjugate gradient method. Our linear system, however, is subjected to noise. The problem itself is not well-conditioned. Thus we choose to use Generalized Minimal Residual Solver (GMRES). The GMRES solver solves the linear system as an optimization problem for each step. The essential element of GMRES solver is the Arnoldi iteration. For each step n, GMRES solver approximates the exact solution $\mathbf{x} = A^{-1}\mathbf{b}$ such that the residual

$$\|\mathbf{r}_n\|_2 = \|A\mathbf{x}_n - \mathbf{b}\|_2, \tag{10}$$

is minimized. GMRES can be regarded as the Krylov subspace method, where the solution $\mathbf{x}$ for each step is a vector in the Krylov subspace K spanned as $\{\mathbf{x}_0, A\mathbf{x}_0, \ldots, A^{n-1}\mathbf{x}_n\}$. Since $\mathbf{x}_n \in K_n$, we can write $\mathbf{x}_n$ as

$$\mathbf{x}_n = K_n\mathbf{c} \tag{11}$$

We can rewrite Eqn. 10 as

$$\|\mathbf{r}_n\|_2 = \|A\mathbf{x}_n - \mathbf{b}\|_2 = \|AK_n\mathbf{c} - \mathbf{b}\|_2 \rightarrow \min \tag{12}$$

We compare the solution to our linear system by using GMRES and the generalized conjugate gradient solver in Fig. 1.

C. Inverse Process: Optimization for Parameter Identification

To estimate the patient-specific relative elasticity, our framework minimizes the error due to approximated parameters in an objective function. Our objective function as defined in

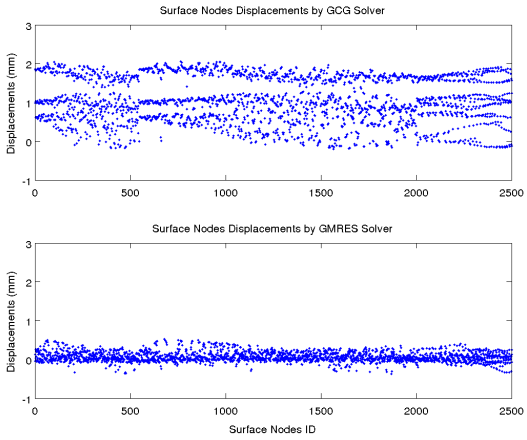

Fig. 1. **Surface Nodes Displacements from GCG Solver and GMRES Solver**. The upper figure shows the surface nodes displacements computed using the Generalized Conjugate Gradiant solver while the bottom figure shows that using the Generalized Minimal Residual Solver. The variation of the displacements computed from GCG solver is larger than the GMRES solver.

Algorithm 1: The main loop of the GMRES solver

```
initialize v_1 = b/||b||;
for n = 1, 2, 3, ... do
    Perform Arnoldi iteration to compute new entries for
     H_n and V_n;
    Find y that minimize ||AV_k y − b||;
end
```

Eqn. 13 consists of the two components. The first part is the difference between the two surfaces – one reconstructed from the reference (initial) set of images, deformed using FEM simulation (as described in Sec. III-B) with the estimated parameters toward the target surface, and one target surface reconstructed from the second set of images. This difference is measured by the Hausdorff distance [31]. In addition we add a Tikhonov regularization [32], [33] term, which improves the conditioning of a possibly ill-posed problem.

With regularization, our objective function is given as:

$$\boldsymbol{\mu} = \underset{\boldsymbol{\mu}}{\operatorname{argmin}} \sum \|\mathbf{d}(\mathbf{S}_l, \mathbf{S}_t)\|^2 + \lambda\boldsymbol{\Gamma}\mathbf{S}_l, \tag{13}$$

with $\mathbf{d}(\mathbf{S}_l, \mathbf{S}_t)$ as the distance between deformed surface and the reference surface, λ as the regularization weight, and $\boldsymbol{\Gamma}$ as the second-order differential operator.

The second-order differential operator $\boldsymbol{\Gamma}$ on a continuous surface (2-manifolds) $\mathbf{S}$ is the curvatures of a point on the surface. The curvature is defined through the tangent plane passing that point. We denote the normal vector of the tangent plane as $\mathbf{n}$ and the unit direction in the tangent plane as $\mathbf{e}_\theta$. The curvature related to the unit direction $\mathbf{e}_\theta$ is $\kappa(\theta)$. The mean curvature κ_{mean} for a continuous surface is defined as, $\kappa_{mean} = \frac{1}{2\pi}\int_0^{2\pi}\kappa(\theta)\mathrm{d}\theta$. The corresponding unit direction $\mathbf{e}_1$ and $\mathbf{e}_2$ are orthogonal to each other. In our implementation, we use triangle mesh to approximate a continuous surface. We use the 1-ring neighbor as the region for computing the mean curvature normal on our discrete surface $\mathbf{S}_l$. We treat each

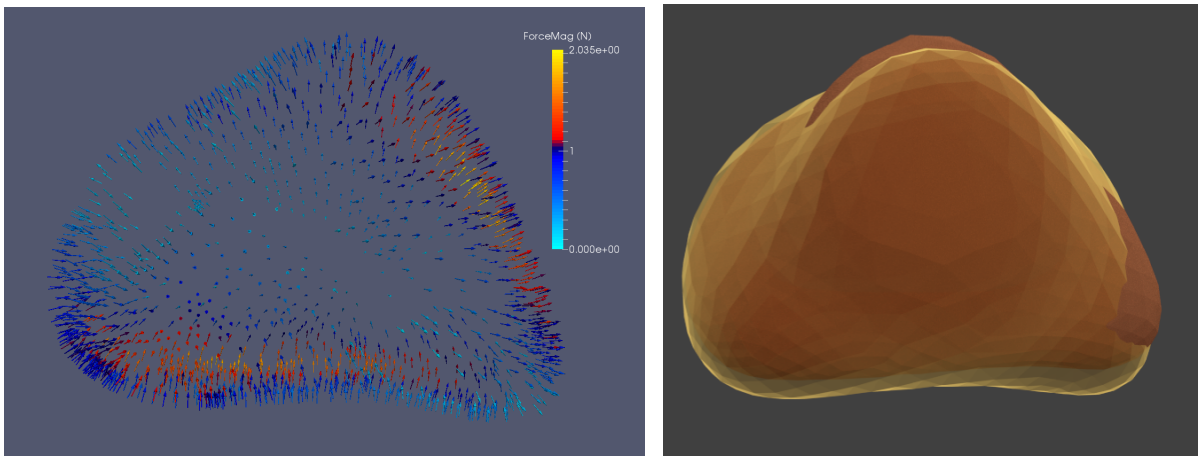

(a) (b)

Fig. 2. **External Force Field and the Overlay of Initial/Target Surfaces**. (a) shows the external force field we recovered. (b) shows the differences between the initial organ surface (solid dark red) and the target surface (transparent yellow).

triangle of the mesh as a local surface with two conformal space parameters u and v. With these two parameters u and v the second-order differential operator $\mathbf{\Gamma}$ on vertex $\mathbf{x}$ is, $\Delta_{u,v}\mathbf{x} = \mathbf{x}_{uu} + \mathbf{x}_{vv}$.

D. Classification Methods

For classification of cancer prognostic scores, we develop a classifier to predict patient cancer T-Stage and Gleason score based on the relative elasticity parameters recovered from CT images. Both the prostate cancer T-stage and the Gleason score are generally considered as ordinal responses. We further compare the effectiveness of ordinal logistic regression [34], multinomial logistic regression [35] and random forests [36] in the context of prostate cancer staging and grading in Sec. IV. We use the RBF kernel to project our feature to higher dimensional space. For oridinal logistic regression, we choose the cumulative logit model. It is also known as the "proportional-odds model". For multinomial or polytomous logistic regression, we use the softmax loss function. We did not directly compare the elasticity with other methods. First of all, ex-vivo methods can substantially change the environment of the organ, resulting in the change of the organ itself. So elasticity parameters cannot be compared directly. Moreover, it is hard to obtain real patient data for testing. Special machines or MR sequences can indeed measure the elasticity in-vivo, but they are not frequently used for routine screening. The reported data in previous literature are also difficult to reproduce. So alternatively we validated our method against synthetic data, where the ground truth values are known precisely.

IV. Patient Data Study

A. Preprocessing and Patient Dataset

Given the CT images (shown in Fig. 3a) of the patient, the prostate, bladder and rectum are first segmented in the images. Then the 3D surfaces (shown in Fig. 3b) of these organs are reconstructed using VTK and these surfaces would be the input to our elasticity parameter reconstruction algorithm. Our patient dataset contains 256 (51 as the reference and 205 as target) sets of CT images from 51 patients, each patient having 2 to 15 sets of CT images. Every patient in the dataset has prostate cancer with cancer T-stage ranging from T1 to T3, Gleason score ranging from 6 to 10, and age from 50 to 85. Gleanson scores are usually used to assess the aggressiveness of the cancer.

B. Cancer Grading/Staging Prediction based on Prostate Elasticity Parameters

We further study the feasibility of using recovered elasticity parameters as a cancer prognostic indicator using our classifier based on relative tissue elasticity values and ages. Two classification methods, ordinal logistic regression (ordinal LR) and multinomial logistic regression (multinomial LR), were tested in our study. We test each method with three sets of features. The first set consists of a single feature, the relative tissue elasticity value $\hat{\mu}$. The second set of features contains both the relative tissue elasticity value and the age. For comparison the third set of features contains only the age information. Our cancer staging has $C = 3$ classes, T1, T2 and T3. And the cancer grading has $G = 5$ classes, from 6 to 10. In our patient dataset, each patient has at least 2 sets of CT images. The elasticity parameter reconstruction algorithm needs 2 sets of CT images as input. We fix one set of CT images as the initial (reference) image and use the other M images. By registering the initial image to the target images, we obtain one elasticity parameter $\hat{\mu}_i, i = 1 \dots M$. We train our classifier on the estimated parameters and perform both per-patient and per-image cross validation.

Per-Image Cross Validation: We treat all the target images ($N = 205$) of all the patients as data points of equal importance. In this experiment, we use leave-one-out cross-validation to evaluate prediction errors of classifiers trained on the three feature sets. Briefly, in each iteration of the cross validation, one image is held out and the classifier is trained on the remaining 204 images. There are 205 such

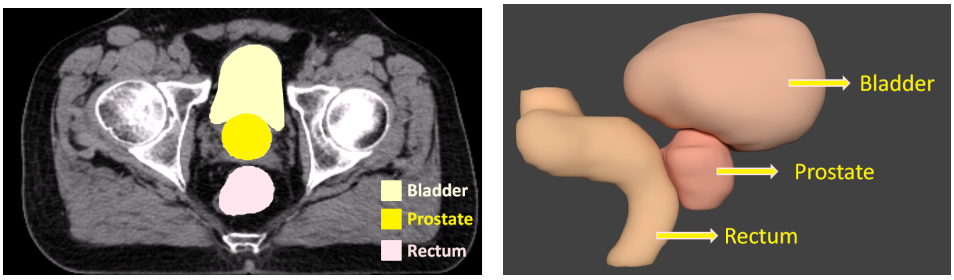

(a) (b)

Fig. 3. **Real Patient CT Image and Reconstructed Organ Surfaces.** (a) shows one slice of the parient CT images with the bladder, prostate and rectum segmented. (b) shows the reconstructed organ surfaces.

iterations, one for each image. The trained classifier's errors on the held-out images are averaged to give the final prediction errors. The results for cancer staging (T-Stage) prediction are shown in Fig. 4a 5a and that for cancer grading (Gleason score) prediction are shown in Fig. 4b 5b. The error metric is measured as the absolute difference between the predicted cancer T-Stage and the actual cancer T-Stage. Zero error-distance means our classifier accurately predicts the cancer T-Stage.

The logistic regression methods (shown in Fig. 4) in general outperforms the random forests method (shown in Fig. 5). And the multinomial method outperforms the ordinal method for both cancer staging (T-Stage) and cancer aggression (Gleason score) prediction. This is because the dimension of the unknown regression coefficients of the multinomial LR for cancer staging classification (with elasticity parameter and age as features) is larger than that of the ordinal LR. With the 'age' feature, we obtain up to $\mathbf{85}\%$ accuracy for predicting cancer T-Stage using multinomial LR method, $\mathbf{82}\%$ using ordinal LR method and 65% using random forests method. For Gleason score prediction we achieve up to $\mathbf{77}\%$ accuracy using multinomial LR method, $\mathbf{62}\%$ using ordinal LR method and 48% using random forests method. Compared to age-only input features, the accuracy using combined features has also largely increased, effectively showing that the estimated elasticity parameter is a critical indicator for predicting the cancer statistics.

Per-Patient Cross Validation: For patients with more than 2 sets of images, we apply Gaussian downsampling kernel to the array $\hat{\mu}_i, i = 1 \dots M$ to compute the sampled elasticity parameter as the elasticity feature of the patient. We first train our classifier using the elasticity feature of the 50 patients then test the trained classifier on the remaining one patient not in the training set. We repeat this process for each of the 51 patients. We also use the three sets of input features described before for comparison. The error distribution for cancer staging (T-Stage) prediction results are shown in Fig. 6a 7a and the error distribution of cancer grading (Gleason score) prediction are shown in Fig. 6b 7b. We observe that the logistic regression methods (shown in Fig. 6) in general outperforms the random forests method (shown in Fig. 7). More interestingly, the age feature helps to increase the prediction accuracy by 10% for staging prediction and 30% for Gleason scoring prediction for the logistic regression methods (both the multinomial and ordinal). But not so much for the random forests classifier. With the age feature, our multinomial classifier achieves up to $\mathbf{82}\%$ accuracy for predicting cancer T-Stage and up to $\mathbf{80}\%$ accuracy for predicting Gleason scores. When the estimated parameter is removed from the feature set, the accuracy has also largely decreased, similar to the per-image study. Our ordinal classifier achieves up to $\mathbf{80}\%$ for cancer T-Stage prediction and $\mathbf{60}\%$ for Gleason score prediction. The random forests classifier obtains 68% for cancer T-Stage prediction (without age information) and 48% for Gleason score prediction (with age information).

Among the 18% failure cases for cancer staging prediction, 15% of our multinomial classifier prediction with age feature is only 1 stage away from the ground truth. And for the failure cases for scoring prediction, only 10% of the predicted Gleason scores is 1 away from the ground truth and 13% of them are 2 away from the ground truth.

V. Conclusion and Future Work

In this paper, we present an improved, non-invasive tissue elasticity parameter reconstruction framework using CT images (that is also applicable to other image modalities). We further studied the correlation of the recovered *relative* elasticity parameters with prostate cancer T-Stage and Gleason score for multiclass classification and prediction of cancer T-stages and grades. The prediction accuracy on our patient dataset using multinormial logistic regression method is up to 84% accurate for predicting cancer T-stages and up to 77% accurate for predicting Gleason scores, which is a lot higher when only using age information. This study further demonstrates the effectiveness of our algorithm for recovering (relative) tissue elasticity parameter *in-vivo* and its potential roles in cancer screening and diagnosis. Other imaging modalities can also be used in our method, as long as the corresponding segmentation and 3D mesh reconstruction algorithm are provided. The main limitation of our method is that the input of our method must be at least two sets of images, with the deformation of the organ between them.

Future Work: This study is performed on 256 sets of images from 51 prostate cancer patients all treated in the same hospital. More image data from more patients can provide a much larger set of training data, thus further improving the training and classification results. Another possible direction is to perform the same study on normal subjects and increase the

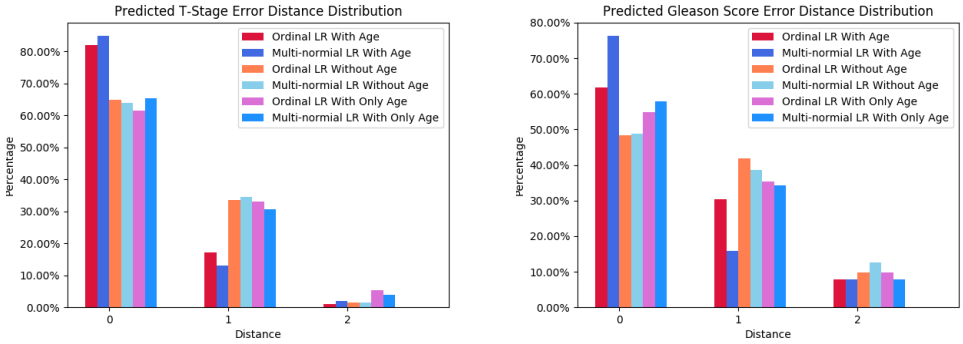

(a) (b)

Fig. 4. **Error Distribution of Cancer Grading/Staging Prediction for Per-Image Study using Logistic Regression Method.** (a) shows error distribution of our cancer staging prediction using the recovered prostate elasticity parameter and the patient's age. For the given patient dataset, the multinomial classifier (shown in royal blue and sky blue), with up to $\mathbf{85\%}$ accuracy, outperforms the ordinal classifier (shown in crimson and coral), with up to $\mathbf{82\%}$ accuracy for predicting cancer T-Stage. (b) shows error distribution of our cancer grading prediction with $\mathbf{77\%}$ accuracy using multinomial LR and $\mathbf{62\%}$ using ordinal LR.

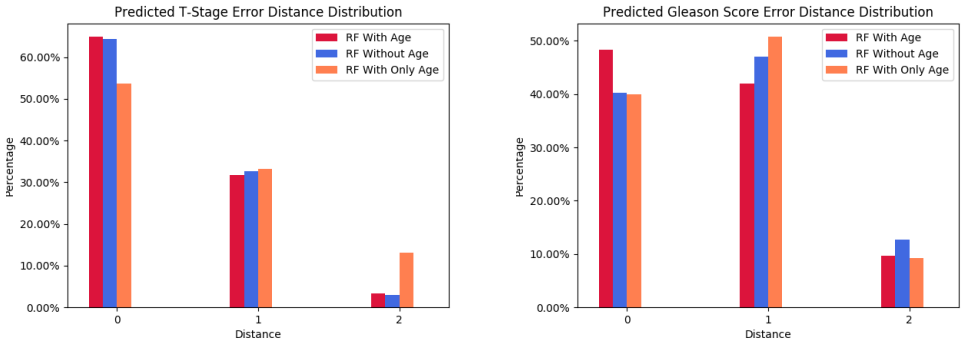

(a) (b)

Fig. 5. **Error Distribution of Cancer Grading/Staging Prediction for Per-Image Study using Random Forests Method.** (a) shows error distribution of the cancer staging prediction using the recovered prostate elasticity parameter with/without the patient's age. For the given patient dataset, the random forests with patient's age (shown in crimson), with up to $\mathbf{65\%}$ accuracy, outperforms the classifier with only the elasticity as the only feature (shown in royal blue), with up to $\mathbf{64\%}$ accuracy for predicting cancer T-Stage. (b) shows error distribution of the cancer grading prediction with $\mathbf{47\%}$ accuracy using both elasticity and age as features and $\mathbf{40\%}$ using only elasticity. Using Random Forest achieves less accuracy than our chosen Logistic Regression methods.

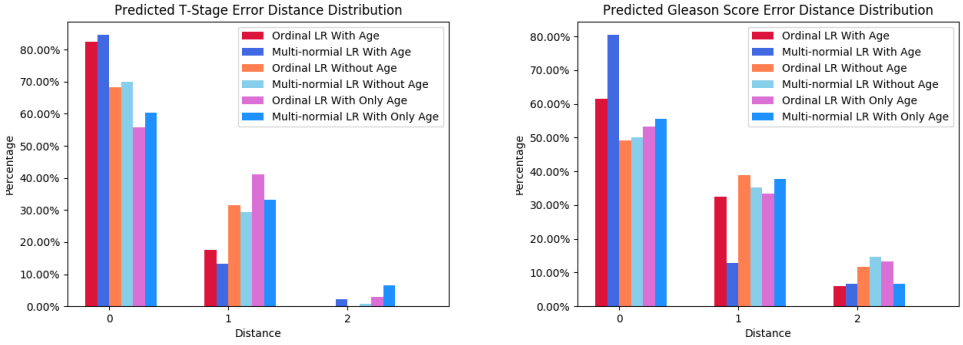

(a) (b)

Fig. 6. **Error Distribution of Cancer Aggression/Staging Prediction for Per-Patient Study using Logistic Regression Methods.** (a) shows the accuracy and error distribution of our recovered prostate elasticity parameter and cancer T-Stage. For our patient dataset, the multinomial classifier, with up to $\mathbf{84\%}$ accuracy (shown in royal blue and sky blue) outperforms the ordinal classifier, with $\mathbf{82\%}$ accuracy (shown in crimson and coral). (b) shows error distribution of our cancer grading prediction with $\mathbf{77\%}$ accuracy using multinomial LR and $\mathbf{70\%}$ using ordinal LR.

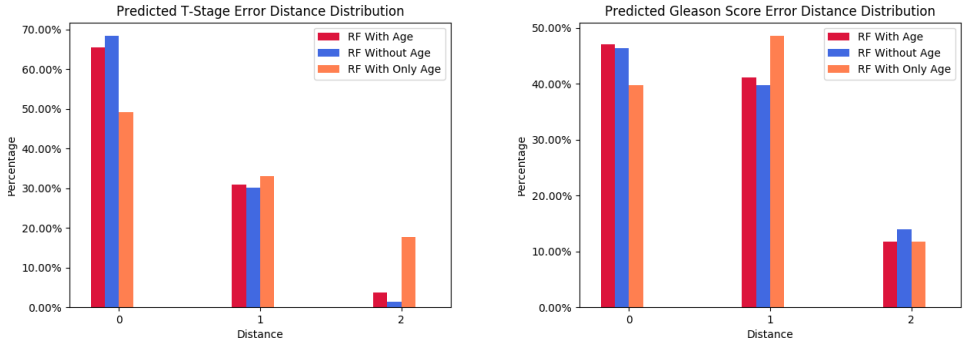

(a) (b)

Fig. 7. **Error Distribution of Cancer Aggression/Staging Prediction for Per-Patient Study using Random Forests Method.** (a) shows error distribution of our cancer staging prediction using the recovered prostate elasticity parameter with/without the patient's age. For our patient dataset, the random forests without patient's age (shown in royal blue), with up to $\mathbf{67\%}$ accuracy, outperforms the classifier with only the elasticity as the only feature (shown in royal crimson), with up to $\mathbf{65\%}$ accuracy for predicting cancer T-Stage. (b) shows error distribution of our cancer grading prediction with $\mathbf{48\%}$ accuracy using both elasticity and age as features and $\mathbf{46\%}$ using only elasticity.

patient diversity from different locations. A large-scale study can enable more complete analysis and lead to more insights on the impact of variability due to demographics and hospital practice on the study results.

REFERENCES

[1] H. A.-D. Ashab, N. F. Haq, G. Nir, P. Kozlowski, P. Black, E. C. Jones, S. L. Goldenberg, S. E. Salcudean, and M. Moradi, "Multimodal classification of prostate tissue: a feasibility study on combining multi-parametric mri and ultrasound," in *SPIE Medical Imaging*. International Society for Optics and Photonics, 2015, pp. 94 141B–94 141B.

[2] A. Khojaste, F. Imani, M. Moradi, D. Berman, D. R. Siemens, E. E. Sauerberi, A. H. Boag, P. Abolmaesumi, and P. Mousavi, "Characterization of aggressive prostate cancer using ultrasound rf time series," in *SPIE Medical Imaging*. International Society for Optics and Photonics, 2015, pp. 94 141A–94 141A.

[3] S. Yang and M. C. Lin, "Materialcloning: Acquiring elasticity parameters from images for medical applications," *IEEE transactions on visualization and computer graphics*, vol. 22, no. 9, pp. 2122–2135, 2016.

[4] O. Goksel, H. Eskandari, and S. E. Salcudean, "Mesh adaptation for improving elasticity reconstruction using the fem inverse problem," *Medical Imaging, IEEE Transactions on*, vol. 32, no. 2, pp. 408–418, 2013.

[5] H.-P. Lee, M. Foskey, M. Niethammer, P. Krajcevski, and M. C. Lin, "Simulation-based joint estimation of body deformation and elasticity parameters for medical image analysis," *Medical Imaging, IEEE Transactions on*, vol. 31, no. 11, pp. 2156–2168, 2012.

[6] K. Shahim, P. Jürgens, P. C. Cattin, L.-P. Nolte, and M. Reyes, "Prediction of cranio-maxillofacial surgical planning using an inverse soft tissue modelling approach," in *Medical Image Computing and Computer-Assisted Intervention–MICCAI 2013*. Springer, 2013, pp. 18–25.

[7] V. Vavourakis, J. H. Hipwell, and D. J. Hawkes, "An inverse finite element u/p-formulation to predict the unloaded state of in vivo biological soft tissues," *Annals of biomedical engineering*, vol. 44, no. 1, pp. 187–201, 2016.

[8] P. Shi and H. Liu, "Stochastic finite element framework for simultaneous estimation of cardiac kinematic functions and material parameters," *Medical Image Analysis*, vol. 7, no. 4, pp. 445–464, 2003.

[9] N. Uniyal, F. Imani, A. Tahmasebi, H. Agarwal, S. Bharat, P. Yan, J. Kruecker, J. T. Kwak, S. Xu, B. Wood *et al.*, "Ultrasound-based predication of prostate cancer in mri-guided biopsy," in *Clinical Image-Based Procedures. Translational Research in Medical Imaging*. Springer, 2014, pp. 142–150.

[10] N. F. Haq, P. Kozlowski, E. C. Jones, S. D. Chang, S. L. Goldenberg, and M. Moradi, "Prostate cancer detection from model-free t1-weighted time series and diffusion imaging," in *SPIE Medical Imaging*. International Society for Optics and Photonics, 2015, pp. 94 142X–94 142X.

[11] ——, "Improved parameter extraction and classification for dynamic contrast enhanced mri of prostate," in *SPIE Medical Imaging*. International Society for Optics and Photonics, 2014, pp. 903 511–903 511.

[12] ——, "A data-driven approach to prostate cancer detection from dynamic contrast enhanced mri," *Computerized Medical Imaging and Graphics*, vol. 41, pp. 37–45, 2015.

[13] A. Davis, K. L. Bouman, J. G. Chen, M. Rubinstein, F. Durand, and W. T. Freeman, "Visual vibrometry: Estimating material properties from small motion in video," in *Proceedings of the IEEE Conference on Computer Vision and Pattern Recognition*, 2015, pp. 5335–5343.

[14] S. Yang, J. Liang, and M. C. Lin, "Learning-based cloth material recovery from video," in *Proceedings of the IEEE Conference on Computer Vision and Pattern Recognition*, 2017, pp. 4383–4393.

[15] S. Yang, V. Jojic, J. Lian, R. Chen, H. Zhu, and M. C. Lin, "Classification of prostate cancer grades and t-stages based on tissue elasticity using medical image analysis," in *International Conference on Medical Image Computing and Computer-Assisted Intervention*. Springer, 2016, pp. 627–635.

[16] H. Delingette, "Toward realistic soft-tissue modeling in medical simulation," *Proceedings of the IEEE*, vol. 86, no. 3, pp. 512–523, 1998.

[17] B. McGinty, www.continuummechanics.org/cm/strain.html, 2012.

[18] P. A. Yushkevich, J. Piven, H. C. Hazlett, R. G. Smith, S. Ho, J. C. Gee, and G. Gerig, "User-guided 3D active contour segmentation of anatomical structures: Significantly improved efficiency and reliability," *NeuroImage*, vol. 31, no. 3, pp. 1116–1128, Jul. 2006.

[19] T. Moons, L. Van Gool, and M. Vergauwen, "3d reconstruction from multiple images," *Foundations and Trends in Computer Graphics and Vision*, vol. 4, no. 4, pp. 287–404, 2010.

[20] N. Snavely, "Bundler v0.9," 2008.

[21] C. Wu, "Visualsfm : A visual structure from motion system," 2013.

[22] H. Si, "Tetgen. a quality tetrahedral mesh generator and three-dimensional delaunay triangulator." 2007.

[23] T. Hu and J. P. Desai, "Characterization of soft-tissue material properties: large deformation analysis," in *Medical Simulation*. Springer, 2004, pp. 28–37.

[24] M. E. Gurtin, *An introduction to continuum mechanics*. Academic press, 1982.

[25] J. Teran, E. Sifakis, G. Irving, and R. Fedkiw, "Robust quasistatic finite elements and flesh simulation," in *Proceedings of the 2005 ACM SIGGRAPH/Eurographics symposium on Computer animation*. ACM, 2005, pp. 181–190.

[26] R. Rivlin, "Large elastic deformations of isotropic materials. iv. further developments of the general theory," *Philosophical Transactions of the Royal Society of London A: Mathematical, Physical and Engineering Sciences*, vol. 241, no. 835, pp. 379–397, 1948.

[27] L. R. Treloar, H. Hopkins, R. Rivlin, and J. Ball, "The mechanics of rubber elasticity [and discussions]," *Proceedings of the Royal Society of London. A. Mathematical and Physical Sciences*, vol. 351, no. 1666, pp. 301–330, 1976.

[28] R. S. Rivlin and D. Saunders, "Large elastic deformations of isotropic materials. vii. experiments on the deformation of rubber," *Philosophical*

Transactions of the Royal Society of London. Series A, Mathematical and Physical Sciences, vol. 243, no. 865, pp. 251–288, 1951.

[29] A. Nava, E. Mazza, F. Kleinermann, N. J. Avis, and J. McClure, "Determination of the mechanical properties of soft human tissues through aspiration experiments," in *Medical Image Computing and Computer-Assisted Intervention-MICCAI 2003*. Springer, 2003, pp. 222–229.

[30] M. Tsutsumi, T. Miyagawa, T. Matsumura, N. Kawazoe, S. Ishikawa, T. Shimokama, T. Shiina, N. Miyanaga, and H. Akaza, "The impact of real-time tissue elasticity imaging (elastography) on the detection of prostate cancer: clinicopathological analysis," *International journal of clinical oncology*, vol. 12, no. 4, pp. 250–255, 2007.

[31] M.-P. Dubuisson and A. K. Jain, "A modified hausdorff distance for object matching," in *Pattern Recognition, 1994. Vol. 1-Conference A: Computer Vision & Image Processing., Proceedings of the 12th IAPR International Conference on*, vol. 1. IEEE, 1994, pp. 566–568.

[32] H. W. Engl, K. Kunisch, and A. Neubauer, "Convergence rates for tikhonov regularisation of non-linear ill-posed problems," *Inverse problems*, vol. 5, no. 4, p. 523, 1989.

[33] G. H. Golub, P. C. Hansen, and D. P. O'Leary, "Tikhonov regularization and total least squares," *SIAM Journal on Matrix Analysis and Applications*, vol. 21, no. 1, pp. 185–194, 1999.

[34] R. Bender and U. Grouven, "Ordinal logistic regression in medical research," *Journal of the Royal College of Physicians of London*, vol. 31, no. 5, pp. 546–551, 1997.

[35] D. Böhning, "Multinomial logistic regression algorithm," *Annals of the Institute of Statistical Mathematics*, vol. 44, no. 1, pp. 197–200, 1992.

[36] L. Breiman, "Random forests," *Machine learning*, vol. 45, no. 1, pp. 5–32, 2001.